PCCP

Accepted Manuscript




ROYAL SOCIETY OF CHEMISTRY

www.rsc.org/pccp

Journal Name

ARTICLE

# Direct Observation of Structural Properties and Fluorescent Trapping Sites in Macrocyclic Porphyrin Arrays at the Single-Molecule Level

Received 00th January 20xx,
Accepted 00th January 20xx

DOI: 10.1039/x0xx00000x

www.rsc.org/

Sujin Ham,[a] Ji-Eun Lee,[a] Suhwan Song,[a] Xiaobin Peng,[b] Takaaki Hori,[b] Naoki Aratani,[b] Atsuhiro Osuka,*[b] Eunji Sim,*[a] and Dongho Kim*[a]

Utilizing single-molecule defocused wide-field fluorescence microscopy, we have investigated the molecular structural properties such as transition dipole moment orientations and the angular relationship among chromophores, as well as structural distortions and flexibilities depending on ring size, in a series of cyclic porphyrin arrays bearing close likeness in overall architectures to the LH2 complexes in purple bacterial photosynthetic systems. Furthermore, comparing the experimental results with molecular dynamics simulations, we ascertained site selection for fluorescent trapping sites. Collectively, these experimental and computational results provide the basis for structure-property relationships and energy hopping/emitting processes in an important class of artificial light-harvesting molecular systems widely used in molecular electronics technology.

## Introduction

Molecular electronics technology has been highlighted across science and technology, providing the possibility of constructing photonic devices at the individual molecular level for device miniaturization.[1-15] The miniaturization of functional materials would essentially bring about molecule-based devices with functionality that could be controlled by the arrangement of constituent functional units. The rational design of molecular devices for photonic, electronic, or optoelectronic applications will require an understanding of the molecular structures and ordering among the constituents in multicomponent macromolecular architectures: this is because of the close relationship between molecular structures and photophysical properties.[16-26]

Various methods have been utilized to reveal molecular structures at the single-molecule level. One such method is defocused wide-field fluorescence microscopy, which provides information on the three-dimensional orientation of the molecular emission dipole moment, from which eventual structural information can be deduced. In comparison with atomic force microscopy[27] and scanning tunneling microscopy,[28] optical spectroscopy enables one to both observe single molecule behavior without strong molecule-substrate interactions and to monitor a variety of dynamic processes in real time.[29] Individual chromophores can emit anisotropic fluorescence in space. Accordingly, the molecular structure of a multichromophoric system can be inferred by analyzing the changes of defocused images in relation to sequential photobleaching processes.[30-44]

Since defocused wide-field imaging (DWFI) measurements are implemented under slightly defocused condition (about 1 μm), porphyrin-based molecular systems have scarcely been studied due to their relatively low fluorescence quantum yields. Nevertheless, inspired by the cyclic arrangement of strongly interacting 9 BChl a dimeric pigments in B850 of LH2,[16-19] there have been numerous synthetic trials to produce molecular architectures that mimic the LH1 and LH2 complexes for fabrication of an artificial light-harvesting apparatus.[20-22] In this regard, cyclic porphyrin arrays have been designed for applications as artificial light-harvesting apparatus,[11,20-25,45-47] because their chemical and physical properties suggest that they will be useful for designing a wide range of molecular devices.[11,46,48-50]

Thus, we prepared a series of cyclic porphyrin arrays (***C**N***Z**s, *N* = 12, 16, 18, 24 and 32; Fig. 1a), in which meso-meso linked Zinc(II) diporphyrin (**Z2**) subunits were bridged by 1,3-phenylene linkers (where *N* is the number of zinc(II) porphyrin monomers).[7,51-52] The constituent building block elements of **Z2** are similar to the BChl dimeric pigments in B850 of LH2. In particular, the cyclic porphyrin arrays **C18Z** resemble the overall structures of the B850 of LH2 complexes.

According to similar absorption and fluorescence spectral features of a series of ***C**N***Z**s (Fig. 1b), we assumed that the dipole coupling strength among **Z2** units is so weak that **Z2** acts as an individual chromophore,[53] i.e., there appear to be six emitting chromophores in **C12Z** as shown in the inset of Fig. 1b.

[a] *Department of Chemistry, Yonsei University, 50, Yonsei-ro, Seodaemun-gu, Seoul, 120-749, Korea.*
[b] *Department of Chemistry, Graduate School of Science, Kyoto University, Sakyo-ku, Kyoto, 606-8502, Japan.*
† Footnotes relating to the title and/or authors should appear here.
Electronic Supplementary Information (ESI) available: [details of any supplementary information available should be included here]. See DOI: 10.1039/x0xx00000x

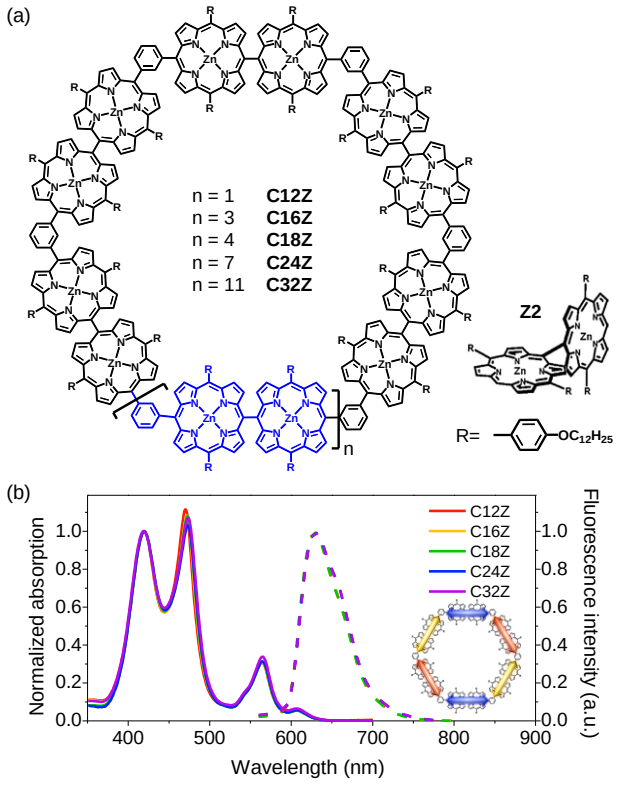


**Fig. 1** (a) Molecular structures of **Z2** and a series of cyclic porphyrin arrays (***CNZ***s). (b) Steady-state absorption (solid lines) and fluorescence (dashed lines) spectra of ***CNZ***s with photoexcitation at 550 nm. The absorption spectra are normalized to the high-energy Soret bands at 420 nm, and fluorescence spectra are normalized to their respective maximum intensities. The inset shows a schematic representation for six emitting chromophores in **C12Z**.

A previous study indicated that excitation energy migration efficiency and structural distortion depend on molecular ring size.[8,53] However, the exact structural properties such as interchromophoric angles and the change of energy emitting sites within these molecules have yet to be thoroughly investigated.

To exclusively reveal the structure-property relationship through a more straightforward approach, DWFI measurements were performed on immobilized ***CNZ***s in a polymeric matrix. The defocused images were captured at the single-molecule level, and then interchromophoric angles were analyzed through vector calculations. After combining this information, we corroborated the relationships between molecular size and structural properties. Furthermore, we compared the experimental results with molecular dynamics (MD) simulations. Based on this analysis, we were able to demonstrate site selection for fluorescent trapping sites; the chromophore next to the first trapping site might be selected as the second trapping site due to the similar nature of the surrounding environment. Such significant information regarding the fluorescent trapping site at the single molecule level is of great interest in its own right, and could lead to in-depth single-molecule studies of related or even larger multichromophoric systems.

## Experimental and Methods

### Ensemble solution spectroscopy

Steady-state absorption spectra were recorded using a UV/Vis spectrometer (Cary5000, Varian). Steady-state emission spectra were recorded using a fluorometer (F- 2500, Hitachi) with an excitation wavelength of 550 nm. Fluorescence quantum yields were measured relative to that of ZnTPP in toluene ($\Phi_F$ = 0.033) with an excitation wavelength of 550 nm. All measurements were performed at room temperature.

### Sample preparation for single-molecule defocused wide-field imaging

Samples for single-molecule measurements were prepared by spin-coating a toluene solution of ***CNZ***s (~$10^{-10}$ M) containing poly(methyl methacrylate) (PMMA) (2 wt %; Sigma-Aldrich, $M_w$ = 996,000) in toluene on rigorously cleaned glass cover slips (~ 100 nm thick, as measured by atomic force microscopy).

### Single-molecule defocused wide-field imaging measurement

Defocused fluorescence imaging measurements were performed using a wide-field fluorescence microscopy system consisting of an inverted optical microscope (IX71, Olympus) equipped with an oil immersion objective (1.4 NA, ×100, Plan Fluorite, Olympus) and a highly sensitive, cooled, 512 × 512 pixels EMCCD camera (Andor, iXon Ultra). For excitation, 445 nm light from a continuous wave laser (Coherent, Cube) with an irradiation power at the sample of approximately 150 W/cm$^2$ was used. The circular polarized laser beam was sent to the microscope after passing through a laser line filter (FF01-445/20-25, Semrock), collimating lens and a dichroic mirror (Di02-R442, Chroma Technology), and was focused onto the back-focal plane of the objective to achieve wide-field illumination (Köhler illumination mode). The defocused fluorescence image was obtained by shifting the sample plane by 0.9 μm toward the objective from the focus position. The defocused image was magnified 3.4 times with a relay lens and spectrally filtered with a notch filter (HNPF-445.0AR-1.0, Kaiser optical system INC.) and band pass filters (BLP01-473R, FF01-496/LP, Semrock). The image integration time was 1 s in order to improve the signal-to-noise ratio. The defocused fluorescence images were analyzed using a pattern matching routine written in the MatLab software to determine the rough transition dipole moment orientation by calculating two-dimensional correlation coefficients ($r$) of the defocused images obtained experimentally (A) and theoretically (B) using Equation 1[32]

$$r = \frac{\sum_m \sum_n (A_{mn} - \bar{A})(B_{mn} - \bar{B})}{\sqrt{(\sum_m \sum_n (A_{mn} - \bar{A})^2)\ (\sum_m \sum_n (B_{mn} - \bar{B})^2)}} \quad (1)$$

where $\bar{A}$ and $\bar{B}$ are the means of A and B, respectively. Furthermore, we have double-checked the defined angles of defocused images every second one by one by comparing with the calculated images to ensure the orientations of the images.

Since the quantum yield of **C12Z** to **C32Z** are between 0.02 and 0.036 which is definitely below the limit for conventional single-molecule detection, the samples were kept under a nitrogen atmosphere to avoid photoinduced oxidation. All measurements were performed in a nitrogen atmosphere at room temperature.

### Molecular dynamics simulation

To further support the ring size dependent conformational changes associated with spectral changes, molecular dynamics (MD) simulations were performed on macrocyclic porphyrin arrays using the NAMD program[56] with the 2b8 version of the CHARMM general force field. The 0.9.7.1 version of the CGenFF program[62-65] was used for efficient parameterization. Because the force field parameters of metal complexes are difficult to generate, zinc atoms inside the porphyrin monomer were mimicked by employing the force constants and angle parameters of the zinc-porphyrin crystal structure in Ref. 66. After several steps of minimization, 3 ns of product run was performed with a 1 fs integration time period. A Langevin thermostat was used to maintain the temperature at $T$=298.15 K during the simulation. The dielectric constant, $\varepsilon_r$ = 2.4, was used for the implicit solvent model of the toluene medium. For further analysis, the atomic coordinates were recorded every 0.5 ps to obtain 6,000 different and uncorrelated molecular conformations from which the interchromophoric angle and planarity parameter distribution were calculated.

### Planarity parameter and angle difference

In this work, the planarity of macrocyclic porphyrin arrays was investigated by means of a planarity parameter, D, such that D approaches 0 as the macrocyclic molecule becomes planar. We employed the least squares plane method[67] to determine the best mean-molecular-plane that minimizes the sum of squares of the distances between almost coplanar atoms and the plane. The planarity parameter was then evaluated as the root-mean-square out-of-plane distance as

$$D = \sqrt{\frac{\sum_i^n (d_i)^2}{n}} \qquad (2)$$

where n is number of atoms used to determine the mean-molecular-plane and $d_i$ is the distance from the $i^{th}$ atom to the plane.

To calculate the interchromophoric angle distribution of ***CNZ*** molecules, we first defined the end-to-end dimer orientation vector for the $i^{th}$ dimer, $\overrightarrow{n_i}$, as shown in Fig. 4b. The interchromophoric angle between the $i^{th}$ and $j^{th}$ dimer is then evaluated utilizing the inner product of $\overrightarrow{n_i}$ and $\overrightarrow{n_j}$. In particular, cosine values between each set of adjacent dimer-dimer subunits are defined as the angle difference, β,

$$\beta = \mathrm{acos}(\overrightarrow{n_i} \cdot \overrightarrow{n_{i+1}}) \qquad (3)$$

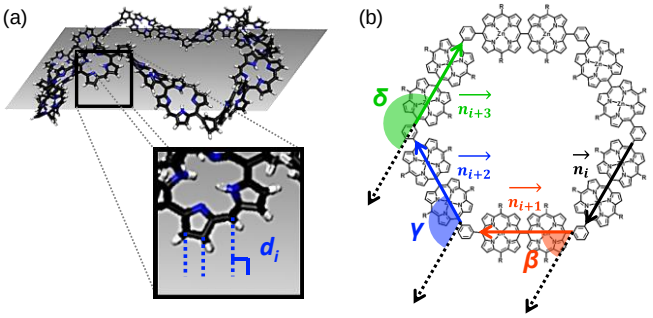


**Scheme 1.** Schematic representation of (a) the planarity parameter and (b) the interchromophoric angles.

while those between non-adjacent dimers are denoted as γ and δ as in Scheme 1b.

## Results and discussion

To investigate the anisotropic emission character of ***CNZ***s, DWFI measurements were performed for single molecules of ***CNZ***s. For excitation, 445 nm light from a continuous wave laser with an irradiation power of approximately 150 W/cm$^2$ at the sample was used. The image integration time was prolonged to 1 s to improve the signal-to-noise ratio. For data analysis, fluorescence intensity trajectories (FITs) were reconstructed from consecutive defocused fluorescence images obtained for each single molecule, after which these defocused images were stacked according to distinct transition dipole moment orientations. The stacked images have a sufficiently enhanced signal-to-noise ratio to define the angles of the observed defocused images.

A typical example is shown in Fig. 2. This single **C12Z** molecule had two distinct fluorescence intensity levels of A and B before permanent photobleaching. Corresponding defocused fluorescence images showed characteristic bilobal emission patterns with different long axis orientations. The dipole orientations of each image are defined by two angles, φ (in-plane) and θ (out-of-plane), which can be determined by matching the observed defocused images with ones calculated

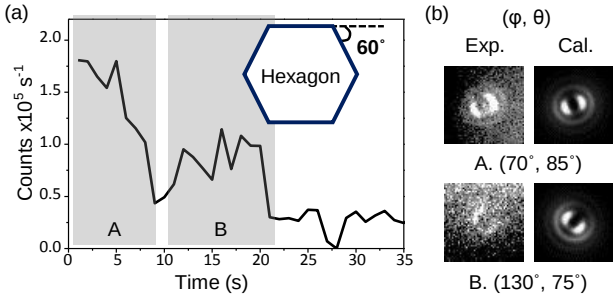


**Fig. 2** Example of defocused wide-field fluorescence imaging measurements from a single **C12Z** molecule. (a) Fluorescence intensity trajectory reconstructed from consecutive defocused images obtained for a single molecule. The trajectory was classified into two intensity levels, A and B. The inset illustrates the two-dimensional regular hexagon. (b) Experimentally observed defocused images (left) and corresponding calculated images (right) for A and B.

using MatLab.[33] Examples with only one emission pattern despite stepwise photobleaching behaviors in FITs are displayed in Fig. S1 in the Supporting Information, which shows the efficient excitation energy hopping processes among **Z2** moieties in **C*N*Z**s.

All defocused images, extracted from approximately 267 FITs for single molecules of **C12Z**, appropriately defined the corresponding transition dipole moments with single orientations; this indicates that the transition dipole moment for **C12Z** is essentially static, leading to polarized emission. If the orientation fluctuated within the image bin time (1 s), the defocused image would appear as an overlap of different emission patterns that cannot determine the orientation by matching with any calculated images.[29,40,42,54] This observation clearly corroborates the validity of theoretical implications that fluorescence emanates from fluorescent trapping sites and that efficient energy transfer occurs towards those sites.

As shown in Fig. 2a, the switch from level A to B is accompanied by an intensity drop due to photobleaching of the constituent **Z2** unit. The transition dipole moments for intensity levels A and B were defined to have angles (ϕ, θ) of (70°, 85°) and (130°, 75°), respectively. The stepwise orientation changes are attributable to energy hopping between identical chromophores emanating from slightly lower-energy chromophores at any moment in time (fluorescent trapping site) due to the inhomogeneous nature of the surrounding polymer matrix.[36,38] After the bleaching of the first trapping site, the chromophore with the next lowest energy emits, and since its orientation is different, a different pattern is observed.[37,40-41]

To evaluate the magnitude of the changes in fluorescence polarization direction, we calculated the angle difference between the transition dipole moments from subsequent intensity levels in the FIT using the law of cosines. The calculated angle difference was 59.8°, in excellent agreement with the value of 60° expected from the two-dimensional hexagonal structure. This example demonstrates that the structural information of a molecule embedded in a solid-state polymer matrix can be inferred by analyzing sequential emission patterns. Further evidence is provided in Fig. S2, which shows representative data for the **C16Z** to **C32Z** molecules.

Fig. 3 shows FITs and defocused images of another **C12Z** molecule displaying continuously decreasing photobleaching behavior, which results from the photobleaching dynamics begin faster than the experimental bin time (1 s). Four sections in the FIT were categorized according to the change in emission patterns. The defined angles are A (335°, 80°), B (25°, 85°), C (340°, 75°), and D (20°, 85°). Particularly noteworthy is that two emission patterns were alternately presented. Defocused images of A and C exhibited no significant difference in the angles of 335° for in-plane and 80° for out-of-plane. Similarity was also observed between the defocused images of B and D. This feature offers the prospect that fluorescence is alternately emitted from two chromophores, suggesting that the two chromophores simultaneously play a role as the fluorescent trapping site. Typical examples of the other molecules, such as **C18Z** and **C24Z**, are shown in Fig. S3. Since chromophores at opposite sides

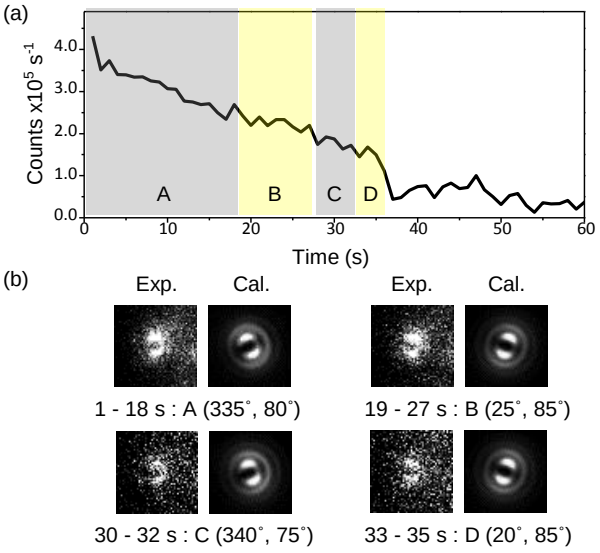


**Fig. 3** Example of the defocused wide-field fluorescence imaging measurements from a single **C12Z** molecule. (a) Fluorescence intensity trajectory reconstructed from consecutive defocused images obtained for a single molecule. The trajectory was classified into two intensity levels A – D. (b) Experimentally observed defocused images (left) and corresponding calculated images (right) for A – D.

of a nonagon can be discerned, **C18Z** strongly suggests not four trapping site, but alternately emitting fluorescence from two chromophores occurs.

On the basis of the above observations, a statistical analysis of experimentally observed interchromophoric angles, α, was carried out by collecting approximately 80 single-molecule datasets for **C*N*Z** to show multiple emission patterns (Fig. 4a). In these series, molecules exhibited fewer distinct orientations during photobleaching than the number of **Z2** units in the **C*N*Z**s because of very weak fluorescence emission due to bleaching of a majority of the absorbing/emitting units[55] or because the energy transfer occurs continuously to the lowest energy trapping site without photobleaching during observation time.[41]

Each histograms were fitted by two Gaussian functions. The left black curves were excluded from our discussions because they would come from fluctuating **Z2** units (Fig. S4). The curve fitted Gaussian function in small angle region (black curve) in the **C12Z** histogram is particularly broad, because **C12Z** has a smaller size and more rigid structure as compared with the other **C*N*Z**s. Accordingly, all six constituent units can act as a fluorescence trapping site due to their close proximities. Theoretically, we can get probabilities of 1/5 for 0° and 4/5 for 60° for α values of perfectly 2-dimensionally planar **C12Z**. As we compare the frequency distributions of **C12Z** located at larger and smaller than 40°, the ratio between the distributions located at larger and smaller than 40° is approximately 1:2. Since not all **C12Z**s have perfectly 2-dimensionally planar structure (slightly tilted and/or distorted), there is difference between theoretical and experimental ratio. We have not included the histogram in the region of 10° to 20°, because the histogram in this region is mainly contributed by the fluctuations of the constituent **Z2** unit (Fig. S4). We think that these

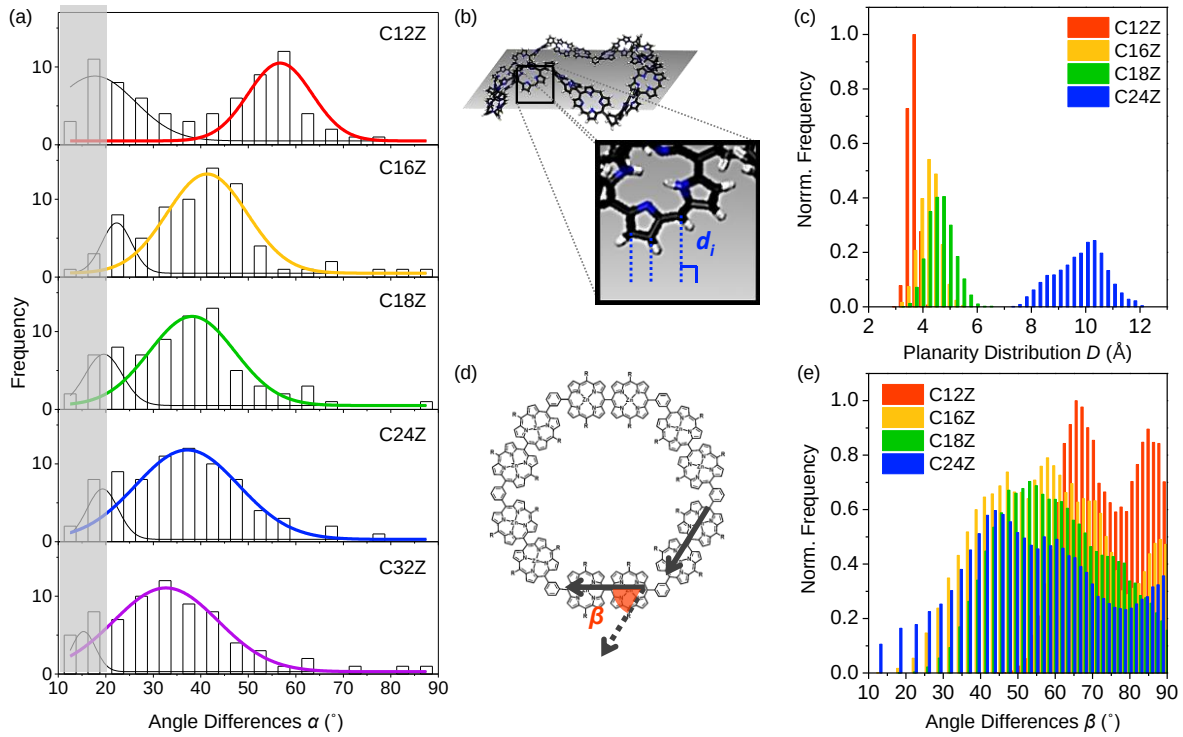


**Fig. 4** (a) Histograms for interchromophoric angles, α, between transition dipole moments from subsequent intensity levels in the fluorescence intensity trajectories for single molecules of ***CNZ***s. The shaded part would come from the fluctuations of **Z2** unit as shown in Fig. S4. Schematics of the (b) planarity parameter and (d) angle differences. Refer to the main text and experimental part for details. Histogram of (c) the planarity parameter, D, and (e) angle differences, β, calculated from 6,000 conformations generated by MD simulations. Refer to the main text and experimental section for details.

features cause the black curve in the **C12Z** histogram becomes particularly broad.

The right curves are centered at 56.8°, 41.6°, 39.3°, 37.2°, and 32.5°, and the full width at half-maximum (FWHM) values are 14.1°, 17.7°, 18.6°, 25.1°, and 25.5° for **C12Z**, **C16Z**, **C18Z**, **C24Z**, and **C32Z**, respectively. The broader distribution in larger *CNZ*s corroborates the increasing flexibility and heterogeneity in larger rings.

Size-dependent conformational disorder is further supported by the existence of various conformers obtained from MD simulation performed with the NAMD program.[56] We took atomic coordinates every 0.5 ps from 3 ns of simulation to obtain 6,000 uncorrelated molecular conformations. To evaluate the planarity of the cyclic backbone, we introduced a planarity parameter, *D*, which represents the average distance per atom from the mean-molecular-plane (Fig. 4b and Scheme 1a). As shown in Fig. 4c, a narrow distribution of **C12Z** approaching small values is the result of two-dimensional planar structures, whereas a broad distribution of **C24Z** with large values is the result of three-dimensional distorted structures. Since **C32Z** molecules have completely distorted structures due to the extremely large molecular size (Fig. S5), we excluded the results of **C32Z** from the distribution of simulated conformers.

It is intriguing that the peak positions of the α values are in good accordance with the interchromophoric angles of regular polygon models (Fig. S6), as well as systematic decrease; However, the α values in large rings are slightly different due to structural nonplanarity as shown in Fig. 4c.[53] The parameters for angle differences are tabulated in Table S1.

There are possible reasons for a good accordance between the experimental and theoretical α values (Fig. S6), as well as a systematic decrease of average α values. The first possible reason is our experimental condition. We used the Köhler illumination mode in our defocused imaging measurements. Since the direction of light propagation is perpendicular to the substrate plane, the excitation of chromophores with an angle θ close to 0° is disfavored[42] and the fluorescence intensity might be too low to detect (C and F in Fig. S7),[57,58] whereas we can easily observe chromophores whose alignments are parallel to the substrate (A, B, D, and E in Fig. S7). Therefore, two adjacent chromophores with a similar angle θ have a high probability of being observed.

However, there are many previous reports supporting preferential alignment of molecules parallel to the substrate, as in the cases of single π-conjugated macrocycles,[28,59] single MEH-PPV chains,[60] and bulk MEH-PPV film.[61] Such preferential alignments are attributed to the shear force exerted during the film spin-coating process.[28,59] In this regard, we think that the Köhler illumination mode would not be a dominant reason.

Second, if the ***CNZ***s have 2-dimensional planar structure, we get probabilities of 1/5 for 0° and 4/5 for 60° for **C12Z**; 1/7 for 0°, 4/7 for 45°, and 2/7 for 90° for **C16Z**; and 1/11 for 0°, 4/11 for 30°, 4/11 for 60°, and 2/11 for 90° for **C24Z**. However, the α values of 90° for **C16Z** and 60° and 90° in **C24Z** were scarcely observed in our histograms (Fig. 4a), Indicating that the ***CNZ***s have not perfectly 2-dimensional planar structures (tilted and/or distorted). Accordingly, not all constituent units act as a fluorescence trapping site.

Third, we suggest that similarities in the surrounding polymeric environment must also be considered. As mentioned before, at any moment a chromophore has the lowest energy due to the inhomogeneous nature of the polymer matrix at the single-molecule level.[41] Although it was impossible to directly indicate the energy level of chromophores embedded in the polymer matrix, the experimental results show the similarity of near polymeric matrix environments.

This point of view was rationalized by the MD simulations which describe the probability distribution for the normalized frequency of a computationally obtained interchromophoric angle, β, between adjacent **Z2** units. As shown in Fig. 4d and 4e, intrachromophoric orientation vectors were defined and angles between the nearest neighbor chromophores were measured. The computed histograms were broader than the experimental ones, presumably because more conformations were used in the MD simulations than the variety of conformations present in actual samples, as well as the larger degrees of freedom in implicit solvent phases (simulated conditions) than in the polymer matrix environments (experimental conditions), and the induced shear force in the process of spin coating.[61]

In Table S1, the mean β values are slightly larger than the mean α values because of the more distorted structures in the simulated condition (Fig. S8). The α and β values, however, have a relatively small difference, as well as similar decreasing tendency and extent. Furthermore, the distributions of non-adjacent interchromophoric angles, γ and δ, of 6,000 MD conformations are presented in Scheme 1b and Fig. S9. Whereas the α and β values have a relatively small difference as well as similar decreasing tendency and extent, Fig. S9 shows a disagreement between the α values and γ or δ values. These results strongly support α values arising from the angles between two adjacent chromophores, β. Based on these results, we think that the fluorescent trapping site was locally selected due to the similar nature of the surrounding environment.

## Conclusions

In summary, a series of porphyrin macrocycles (**C*N*Z**s) have been investigated by defocused fluorescence imaging measurements and MD simulations with a focus on molecular structural information. The obtained structural parameters enabled us to determine the orientations of transition dipole moments and interchromophoric angles. Our findings suggest that the molecular heterogeneities and flexibilities of **C*N*Z**s clearly depend on the ring size; as the ring size becomes larger, **C*N*Z**s become more distorted. Furthermore, we discovered site selection for the fluorescent trapping site in single multichromophoric macrocycles by a comparative analysis between experimental and computational results; the chromophore adjacent to the first fluorescent trapping site has a high probability of being selected as the second fluorescent trapping site due to the similar nature of the surrounding environment. The direct observation of prevailing molecular conformations and the location of fluorescent trapping sites in multichromophoric macrocycles using single-molecule spectroscopic methods provides not only a new level of understanding, but will also stimulate other experimental and computational studies on related multichromophoric systems.

## Acknowledgements

The work at Yonsei University was supported by Global Research Laboratory (2013K1A1A2A02050183) through the National Research Foundation of Korea (NRF) funded by the Ministry of Science, ICT (Information and Communication Technologies) and Future Planning (D.K.). This work at Kyoto was supported by JSPS KAKENHI Grant Numbers No. 25220802 and 25620031.

## References

1 T. Basch, W. E. Moerner, M. Orrit and U. P. Wild, *Single Molecule Optical Detection, Imaging and Spectroscopy,* Wiley-VCH, Weinheim, 1997.
2 B. Lounis and W. E. Moerner, *Nature*, 2000, **407**, 491-493.
3 M. Irie, T. Fukaminato, T. Sasaki, N. Tamai and T. Kawai, *Nature*, 2002, **420**, 759-760.
4 F. C. De Schryver, T. Vosch, M. Cotlet, M. Van Der Auweraer, K. Müllen and J. Hofkens, *Acc. Chem. Res.*, 2005, **38**, 514-522.
5 P. Tinnefeld and M. Sauer, *Angew. Chem. Int. Ed.*, 2005, **44**, 2642-2671.
6 M. F. García-Parajó, J. Hernando, G. S. Mosteiro, J. P. Hoogenboom, E. M. H. P. Van Dijk and N. F. Van Hulst, *ChemPhysChem*, 2005, **6**, 819-827.
7 M. Park, M. C. Yoon, Z. S. Yoon, T. Hori, X. Peng, N. Aratani, J. I. Hotta, H. Uji-I, M. Sliwa, J. Hofkens, A. Osuka and D. Kim, *J. Am. Chem. Soc.*, 2007, **129**, 3539-3544.
8 J. Yang, M. Park, Z. S. Yoon, T. Hori, X. Peng, N. Aratani, P. Dedecker, J. Hotta, H. Uji-i, M. Sliwa, J. Hofkens, A. Osuka, D. Kim, *J. Am. Chem. Soc.*, 2008, **130**, 1879-1884.
9 H. Jin, D. A. Heller, J. H. Kim and M. S. Strano, *Nano Lett.*, 2008, **8**, 4299-4304.
10 R. W. Wagner and J. S. Lindsey, *J. Am. Chem. Soc.*, 1994, **116**, 9759-9760.
11 D. Holten, D. F. Bocian and J. S. Lindsey, *Acc. Chem. Res.*, 2002, 57-69.
12 H. L. Anderson, *Inorg. Chem.*, 1994, **33**, 972-981.
13 M. P. Debreczeny, W. A. Svec and M. R. Wasielewski, *Science*, 1996, **274**, 584-587.
14 R. E. Martin and F. Diederich, *Angew. Chem. Int. Ed.*, 1999, **38**, 1350-1377.
15 G. D. Scholes, K. P. Ghiggino, A. M. Oliver and M. N. Paddon-Row, *J. Am. Chem. Soc.*, 1993, **115**, 4345-4349.
16 A. W. Roszak, T. D. Howard, J. Southall, A. T. Gardiner, C. J. Law, N. W. Isaacs and R. J. Cogdell, *Science*, 2003, **302**, 1969-1972.
17 G. McDermott, S. M. Prince, A. A. Freer, A. M. Hawthornthwaite-Lawless, M. Z. Papiz, R. J. Cogdell and N. W. Isaacs, *Nature*, 1995, 374, 517-521.
18 A. Freer, S. Prince, K. Sauer, M. Papiz, A. Hawthornthwaite-Lawless, G. McDermott, R. Cogdell and N. W. Isaacs, *Structure*, 1996, **4**, 449-462.
19 C. Jungas, J. L. Ranck, J. L. Rigaud, P. Joliot and A. Verméglio, The *EMBO J.*, 1999, **18**, 534-542.
20 H. A. M. Biemans, A. E. Rowan, A. Verhoeven, P. Vanoppen, L. Latterini, J. Foekema, A. P. H. J. Schenning, E. W. Meijer, F. C. De Schryver and R. J. M. Nolte, *J. Am. Chem. Soc.*, 1998, **120**, 11054-11060.

21 J. Li, A. Ambroise, S. I. Yang, J. R. Diers, J. Seth, C. R. Wack, D. F. Bocian, D. Holten and J. S. Lindsey, *J. Am. Chem. Soc.*, 1999, **121**, 8927-8940.
22 C. M. Drain, F. Nifiatis, A. Vasenko and J. D. Batteas, *Angew. Chem. Int. Ed.*, 1998, **37**, 2344-2347.
23 S. Anderson, H. L. Anderson and J. K. M. Sanders, *Acc. Chem. Res.*, 1993, **26**, 469-475.
24 P. Brodard, S. Matzinger, E. Vauthey, O. Mongin, C. Papamicaël and A. Gossauer, *J. Phys. Chem. A*, 1999, **103**, 5858-5870.
25 R. Takahashi and Y. Kobuke, *J. Am. Chem. Soc.*, 2003, **125**, 2372-2373.
26 M. R. Wasielewski, *Chem. Rev.*, 1992, **92**, 435-461.
27 F. Schlosser, V. Stepanenko and F. Würthner, *Chem. Commun.,* 2010, **46**, 8350-8352.
28 A. V. Aggarwal, A. Thiessen, A. Idelson, D. Kalle, D. Würsch, T. Stangl, F. Steiner, S. S. Jester, J. Vogelsang, S. Höger and J. M. Lupton, *Nat. Chem.*, 2013, **5**, 964-70.
29 S. Ham, J. Yang, F. Schlosser, F. Würthner and D. Kim, *J. Phys. Chem. Lett.,* 2014, **5**, 2830-2835.
30 P. Dedecker, B. Muls, A. Deres, H. Uji-I, J. I. Hotta, M. Sliwa, J. P. Soumillion, K. Müllen, J. Enderlein and J. Hofkens, *Adv. Mater.*, 2009, **21**, 1079-1090.
31 M. Böhmer and J. Enderlein, *J. Opt. Soc. Am. B*, 2003, **20**, 554-559.
32 S. Habuchi, T. Oba and M. Vacha, *Phys. Chem. Chem. Phys.*, 2011, **13**, 7001-7007.
33 D. Patra, I. Gregor and J. Enderlein, *J. Phys. Chem. A*, 2004, **108**, 6836-6841.
34 J. Enderlein, *Opt. Lett.*, 2000, **25**, 634-636.
35 A. P. Bartko and R. M. Dickson, *J. Phys. Chem. B*, 1999, **103**, 3053-3056.
36 A. P. Bartko and R. M. Dickson, *J. Phys. Chem. B*, 1999, **103**, 11237-11241.
37 R. M. Dickson, D. J. Norris and W. E. Moerner, *Phys. Rev. Lett.*, 1998, **81**, 5322-5325.
38 A. Cyphersmith, A. Maksov, R. Hassey-Paradise, K. D. McCarthy and M. D. Barnes, *J. Phys. Chem. Lett.*, 2011, **2**, 661-665.
39 W. Schroeyers, R. Vallée, D. Patra, J. Hofkens, S. Habuchi, T. Vosch, M. Cotlet, K. Müllen, J. Enderlein and F. C. De Schryver, *J. Am. Chem. Soc.*, 2004, **126**, 14310-14311.
40 S. M. Melnikov, E. K. L. Yeow, H. Uji-i, M. Cotlet, K. Müllen, F. C. De Schryver, J. Enderlein and J. Hofkens, *J. Phys. Chem. B*, 2007, **111**, 708-719.
41 J. Hofkens, M. Maus, T. Gensch, T. Vosch, M. Cotlet, F. Köhn, A. Herrmann, K. Müllen and F. De Schryver, *J. Am. Chem. Soc.*, 2000, **122**, 9278-9288.
42 J. A. Hutchison, H. Uji-I, A. Deres, T. Vosch, S. Rocha, S. Müller, A. A. Bastian, J. Enderlein, H. Nourouzi, C. Li, A. Herrmann, K. Müllen, F. De Schryver and J. Hofkens, *Nat. Nanotechnol.*, 2014, **9**, 131-136.
43 A. Deres, G. A. Floudas, K. Müllen, M. Van Der Auweraer, F. De Schryver, J. Enderlein, H. Uji-I and J. Hofkens, *Macromolecules*, 2011, **44**, 9703-9709.
44 T. Motegi, H. Nabika, Y. Niidome and K. Murakoshi, *J. Phys. Chem. C*, 2013, **117**, 2535-2540.
45 D. Gust, T. A. Moore and A. L. Moore, *Acc. Chem. Res.*, 2001, **34**, 40-48.
46 D. Kim and A. Osuka, *Acc. Chem. Res.*, 2004, **37**, 735-745.
47 A. Prodi, C. Chiorboli, F. Scandola, E. Iengo, E. Alessio, R. Dobrawa and F. Würthner, *J. Am. Chem. Soc.*, 2005, **127**, 1454-1462.
48 K. Kadish, K. M. Smith and R. Guilard, *The Porphyrin Handbook Vol. 6,* Academic Press, New York, 1999.
49 H. L. Anderson, S. J. Martin and D. D. C. Bradley, *Angew. Chem. Int. Ed.,* 1994, **33**, 655-657.
50 G. Di Santo, C. Sfiligoj, C. Castellarin-Cudia, A. Verdini, A. Cossaro, A. Morgante, L. Floreano and A. Goldoni, *Chem. Eur. J.*, 2012, **18**, 12619-12623.
51 X. Peng, N. Aratani, A. Takagi, T. Matsumoto, T. Kawai, I. W. Hwang, T. K. Ahn, D. Kim and A. Osuka, *J. Am. Chem. Soc.*, 2004, **126**, 4468-4469.
52 T. Hori, N. Aratani, A. Takagi, T. Matsumoto, T. Kawai, M. C. Yoon, Z. S. Yoon, S. Cho, D. Kim, and A. Osuka, *Chem. Eur. J.*, 2006, **12**, 1319-1327.
53 M. C. Yoon, S. Cho, P. Kim, T. Hori, N. Aratani, A. Osuka and D. Kim, *J. Phys. Chem. B*, 2009, **113**, 15074-15082.
54 E. Da Como, K. Becker, J. Feldmann and J. M. Lupton, *Nano Lett.*, 2007, **7**, 2993-2998.
55 J. Yang and D. Kim, *J. Mater. Chem.*, 2009, **19**, 1057-1062.
56 J. C. Phillips, R. Braun, W. Wang, J. Gumbart, E. Tajkhorshid, E. Villa, C. Chipot, R. D. Skeel, L. Kalé and K. Schulten, *J. Comput. Chem.*, 2005, **26**, 1781-1802.
57 S. Krause, D. Kowerko, R. Börner, C. G. Hübner and C. Von Borczyskowski, *ChemPhysChem*, 2011, **12**, 303-312.
58 R. Börner, D. Kowerko, S. Krause, C. Von Borczyskowski and C. G. Hübner, *J. Chem. Phys.*, 2012, **137,** 164202.
59 I. G. Scheblykin, *Nat. Chem.*, 2013, **5**, 903-904.
60 Y. Ebihara and M. Vacha, *J. Phys. Chem. B*, 2008, **112**, 12575-12578.
61 I. M. Craig, C. J. Tassone, S. H. Tolbert and B. J. Schwartz, *J. Chem. Phys.*, 2010, **133**, 044901.
62 K. Vanommeslaeghe, E. Hatcher, C. Acharya, S. Kundu, S. Zhong, J. Shim, E. Darian, O. Guvench, P. Lopes, I. Vorobyov, A. D. MacKerell Jr., *J. Comput. Chem.* 2010, **31**, 671-690.
63 W. Yu, X. He, K. Vanommeslaeghe and A. D. MacKerell, *Jr., J. Comput. Chem.*, 2012, **33**, 2451-2468.
64 K. Vanommeslaeghe and a. D. MacKerell Jr., *J. Chem. Inf. Model.*, 2012, **52**, 3144-3154.
65 K. Vanommeslaeghe, E. Prabhu Raman, A. D. MacKerell, Jr., *J. Chem. Inf. Model.* 2012, **52**, 3155-3168.
66 H. M. Marques and I. Cukrowski, *Phys. Chem. Chem. Phys.*, 2002, **4**, 5878-5887.
67 F. J. Burkowski, *Computational and Visualization Techniques for Structural Bioinformatics Using Chimera,* Chapman & Hall/CRC Mathematical and Computational Biology, 2014, pp. 154-165.